








# Integrated RMP-based ELM-crash-control process for plasma performance enhancement during ELM crash suppression in KSTAR

Minwoo Kim<sup>1,\*</sup> , G. Shin<sup>1</sup> , J. Lee<sup>1</sup> , W.H. Ko<sup>1</sup>, H. Han<sup>1</sup> , S.-H. Hahn<sup>1</sup> , S.K. Kim<sup>2,3</sup> , S.M. Yang<sup>3</sup> , R. Shousha<sup>2,3</sup> , H.S. Kim<sup>1</sup>, J.-W. Juhn<sup>1</sup> , G.Y. Park<sup>1</sup> and E. Kolemen<sup>2,3</sup>

<sup>1</sup> Korea Institute of Fusion Energy, Daejeon, 34133, Korea, Republic Of

<sup>2</sup> Princeton University, Princeton, NJ 08544, United States of America

<sup>3</sup> Princeton Plasma Physics Laboratory, Princeton, NJ 08543-0451, United States of America

E-mail: [minwookim@kfe.re.kr](mailto:minwookim@kfe.re.kr)

Received 9 March 2023, revised 23 June 2023

Accepted for publication 5 July 2023

Published 18 July 2023



## Abstract

The integrated Resonant Magnetic Perturbation (RMP)-based Edge-Localized Mode (ELM)-crash-control process aims to enhance the plasma performance during the RMP-driven ELM crash suppression, where the RMP induces an unwanted confinement degradation. In this study, the normalized beta ( $\beta_N$ ) is introduced as a metric for plasma performance. The integrated process incorporates the latest achievements in the RMP technique to enhance  $\beta_N$  efficiently. The integrated process triggers the  $n = 1$  Edge-localized RMP (ERMP) at the L–H transition timing using the real-time Machine Learning (ML) classifier. The pre-emptive RMP onset can reduce the required external heating power for achieving the same  $\beta_N$  by over 10% compared to the conventional onset. During the RMP phase, the adaptive feedback RMP ELM controller, demonstrating its performance in previous experiments, plays a crucial role in maximizing  $\beta_N$  during the suppression phase and sustaining the  $\beta_N$ -enhanced suppression state by optimizing the RMP strength. The integrated process achieves  $\beta_N$  up to  $\sim 2.65$  during the suppression phase, which is  $\sim 10\%$  higher than the previous KSTAR record but  $\sim 6\%$  lower than the target of the K-DEMO first phase ( $\beta_N = 2.8$ ), and maintains the suppression phase above the lower limit of target  $\beta_N (= 2.4)$  for  $\sim 4$  s ( $\sim 60\tau_E$ ). In addition to  $\beta_N$  enhancement, the integrated process demonstrates quicker restoration of the suppression phase and recovery of  $\beta_N$  compared to the adaptive control with the  $n = 1$  Conventional RMP (CRMP). The post-analysis of the experiment shows the localized effect of the ERMP spectrum in radial and the close relationship between the evolution of  $\beta_N$  and the electron temperature.

\* Author to whom any correspondence should be addressed.



Original Content from this work may be used under the terms of the [Creative Commons Attribution 4.0 licence](https://creativecommons.org/licenses/by/4.0/). Any further distribution of this work must maintain attribution to the author(s) and the title of the work, journal citation and DOI.

Keywords: ELMs, RMP, real-time ELM control, normalized beta, KSTAR

(Some figures may appear in colour only in the online journal)

## 1. Introduction

The steep pressure gradient and the high current density at the edge of High-Performance Mode (H-mode) plasma drive quasi-periodic pedestal relaxation, the so-called Edge-Localized Mode (ELM) crash. The ELM crash generates heat and particle flux onto Plasma-Facing Components (PFC), which can threaten machine safety in ITER [1] and post-ITER tokamaks. An applying external magnetic perturbation resonant at the rational surface(s), called Resonant Magnetic Perturbation (RMP), is proposed to control ELM crashes [2, 3]. Various tokamaks realize the RMP-driven ELM crash suppression, allowing tokamak machines to relieve the mechanical stress: KSTAR [4–6], DIII-D [2, 7–9], ASDEX Upgrade [10, 11], and EAST [12]. However, the RMP technique is associated with an unwanted plasma performance degradation primarily caused by RMP-induced density pump-out, which is experimentally observed in multiple machines, including KSTAR [13–15], DIII-D [16–19], ASDEX Upgrade [11, 20], MAST [21, 22], and EAST [23, 24], and reproduced by simulations [25–27].

Despite the performance degradation induced by the RMP, the RMP spectra reliably suppress ELM crashes within the suppression window. KSTAR can produce various external magnetic perturbation spectra using three rows of in-vessel coils in the poloidal direction and four window-pane-like coils at each row in the toroidal direction [28]. Among many different combinations of coil current in each row and phasing (phase difference of lower-row coil to adjacent upper-row coil), the Non-Resonant Magnetic Perturbation (NRMP), almost orthogonal to the helical field lines, brakes the plasma rotation only without obvious density pump out [29–31]. The Quasi-Symmetric Magnetic Perturbation (QSMP), restoring quasi-symmetry of perturbed particle orbit, has little effect on plasma density and rotation [30]. However, neither NRMP nor QSMP suppresses ELM crashes. Moreover, according to an analysis of DIII-D plasmas without ELM crashes, the RMP plasmas can have advantages over other operating regimes, such as enhanced  $D_\alpha$  H-mode (EDA-H), improved energy confinement mode (I-mode), and quiescent H-mode (QH-mode), in terms of the plasma performance [32]. This paper focuses specifically on enhancing plasma performance during the RMP-driven ELM-crash-suppression phase. In order to adopt the RMP technique in ITER and future fusion devices, it is required to recover and enhance the plasma performance during the suppression phase.

A database for KSTAR RMP-driven ELM-crash-control experiments is constructed to investigate experimental conditions favorable to the plasma performance enhancement in the ELM-crash-suppression phase. Here, the normalized beta ( $\beta_N$ ) represents the plasma performance, where  $\beta_N = \beta \cdot aB_T/I_p$ , and  $\beta = \langle p \rangle / (B^2/2\mu_0)$ . The  $\beta_N$  of performance-enhanced plasmas can be compared to whether it approaches the target

$\beta_N$  of a demonstration fusion power plant (DEMO) design (2.8 in the K-DEMO first phase [33], 2.6 and 3.8 in the EU DEMO1 and DEMO2 design options [34], and 3.4 in the JA DEMO steady-state plasma [35]). The database analysis indicates that the auxiliary heating power ( $P_{\text{heat}}$ ) and the RMP coil current ( $I_{\text{RMP}}$ ) are the two most relevant factors determining  $\beta_N$  during the RMP-driven suppression phase. The basic approach to  $\beta_N$  enhancement is to increase  $P_{\text{heat}}$  to the maximum available value and to reduce  $I_{\text{RMP}}$  to around the suppression threshold. However, for an efficient and stable  $\beta_N$ -enhanced suppression phase, it is necessary to introduce the latest achievements related to the RMP technique. The pre-emptive RMP onset based on the real-time Machine Learning (ML) classifier [36], which automatically triggers RMP before the first ELM after the L–H transition, can obtain a higher ion temperature at the plasma core region compared to the conventional pre-set RMP onset [37]. The interactive  $I_{\text{RMP}}$  control by the adaptive feedback RMP ELM controller balances  $\beta_N$  enhancement and ELM crash suppression by optimizing  $I_{\text{RMP}}$  [15, 38, 39], in contrast to the conventional pre-set  $I_{\text{RMP}}$  control. The optimization of not only  $I_{\text{RMP}}$  for the RMP strength but also the RMP spectrum can contribute favorably to plasma confinement. The Edge-localized RMP (ERMP) spectrum has a high enough edge resonant magnetic field to suppress ELM crashes while reducing the resonant field in the core region compared to the Conventional RMP (CRMP) spectrum [40, 41]. The accomplishments mentioned above are combined into the integrated RMP-based ELM-crash-control process. The main body of the paper will provide a detailed description and achievements of the integrated process.

The outline of this paper is as follows. Section 2 analyzes the  $\beta_N$  database for KSTAR RMP-driven ELM-crash-control experiments. Section 3 describes the experimental plan for efficient  $\beta_N$  enhancement during the suppression phase. Section 4 reports the achievement of the integrated RMP-based ELM-crash-control process in enhancing  $\beta_N$  and the post-analysis results. Section 5 presents a plan for expanding the integrated process to plasma performance-enhanced long-pulse ELM-less operation. Finally, section 6 gives a summary of this paper.

## 2. $\beta_N$ database for KSTAR RMP-driven ELM-crash-control experiments

KSTAR demonstrates robust and reproducible RMP-driven ELM crash suppression [4, 13, 14, 42–44], thereby contributing to understanding the suppression mechanism [5, 45] and expecting the suppression window in the RMP coil phase-space [46]. Based on this reliability of the RMP-driven suppression in KSTAR, a database for KSTAR RMP-driven ELM-crash-control experiments is constructed to study the plasma performance during the RMP phase, where  $\beta_N$

represents the plasma confinement performance and all the discharges are in a Lower Single Null (LSN) configuration. The  $\beta_N$  database tabulates the following information:  $B_T$  (toroidal magnetic field strength at the geometrical axis), plasma current ( $I_p$ ), RMP configuration [toroidal harmonic number ( $n$ ), RMP coil phasing, and coil current ( $I_{RMP}$ )], magnetic EFIT data [47] [safety factor at 95% of normalized toroidal magnetic flux ( $q_{95}$ ), plasma elongation ( $\kappa$ ), plasma triangularity ( $\delta_u$ , and  $\delta_l$ ),  $\beta_N$ , and  $W_{MHD}$ ], line-averaged density ( $n_{e,l}$ ) from mm-wave interferometry [48] and two-color interferometry (TCI) [49], total Neutral Beam Injection (NBI) power ( $P_{NBI}$ ), and total electron cyclotron heating (ECH) power ( $P_{ECH}$ ). The RMP configuration of the discharges included in the database is categorized into two groups: static  $n = 1$ ,  $+90^\circ$  phasing [4] (207 shots) and static  $n = 2$ ,  $+90^\circ$  phasing [6] (76 shots). For reference, in KSTAR, the four window-pane-like RMP coils in the toroidal direction can generate magnetic perturbation up to  $n = 2$ . The database includes 283 RMP-driven ELM-crash-control discharges and 2067 data sets, of which 169 are ELM-crash-suppression discharges (119 cases for  $n = 1$  RMP, and 50 cases for  $n = 2$  RMP) and 557 are the suppression data sets (387 cases for  $n = 1$  RMP, and 170 cases for  $n = 2$  RMP). Each data set comprises a collection of time-averaged values for the parameters listed above. The time of interest is selected based on three criteria: 1) Within the time-averaging period of  $\pm 0.1$  s around the chosen time point, the ELM crash patterns affected by the RMP remain stable, regardless of whether the RMP entirely suppresses ELM crashes. 2) The plasma equilibrium has no unintended perturbations during this period. 3) The measurement data is reliable and free of excessive noise. The database excludes the rotating RMP configuration, where the relative phase to the laboratory frame changes in time. This is because the rotating RMP perturbs equilibrium conditions despite constant RMP strength and phasing [43].

The suppression data sets provide the relationship between  $\beta_N$  and parameters listed in the database during the ELM-crash-suppression period. As shown in figure 1(a), in the  $n = 1$  RMPs,  $\beta_N$  positively correlates with the total auxiliary heating power ( $P_{heat} = P_{NBI} + P_{ECH}$ ). In the  $n = 2$  RMPs (figure 1(b)), it seems that  $\beta_N$  is insensitive to  $P_{heat}$ . However, the  $n = 2$  RMP experiments are conducted in a wide  $I_p$  range different from the  $n = 1$  RMP experiments (figure 2). Since  $\beta_N$  is inversely proportional to  $I_p$  by definition, it is necessary to decouple the  $I_p$  effect on  $\beta_N$  to investigate the relationship between  $\beta_N$  and  $P_{heat}$  in the  $n = 2$  RMPs. In both two majority  $I_p$  ranges of the  $n = 2$  RMPs ( $550 \leq I_p \leq 620$  kA, and  $730 \leq I_p \leq 800$  kA),  $\beta_N$  increases as  $P_{heat}$  increases (figure 3). For reference, the NBI in co- $I_p$  direction and the ECH are the main heating sources in KSTAR, but about 91% (153 shots) of the suppression discharges in the database use the NBI only.

In this study,  $I_{RMP}$  represents the strength of the resonant magnetic field ( $|\delta B_{res}|$ ). However,  $|\delta B_{res}|$  can vary at the same  $I_{RMP}$  due to the plasma response to external magnetic perturbation, which is influenced by plasma conditions such as magnetic shear, temperature, and density profiles. Although the precise calculations considering the plasma response can

provide exact resonant magnetic field ( $\delta B_{res}$ ) spectra, such calculations are not available for all the cases in the database. In both  $n = 1$  and  $n = 2$  RMP configurations, an increase in  $I_{RMP}$  tends to decrease  $\beta_N$  (figure 4), although the effects of  $I_p$  (especially  $n = 2$  RMPs) and  $P_{heat}$  on  $\beta_N$  are not decoupled from that of  $I_{RMP}$ . In the  $n = 1$  RMPs, the  $\beta_N$  reduction slope is steeper than the  $n = 2$  RMPs. The observed trend appears to be due to the differences in  $\delta B_{res}$  spectra, such as the penetration depth into the plasma core, between  $n = 1$  and  $n = 2$  RMPs. However, it is not possible to directly compare  $\delta B_{res}$  spectra or  $|\delta B_{res}|$  of  $n = 1$  and  $n = 2$  RMPs using  $I_{RMP}$ .

The database analysis shows that  $P_{heat}$  and  $I_{RMP}$  are the most influential parameters on  $\beta_N$  of the suppression phase. In contrast to  $P_{heat}$  and  $I_{RMP}$ , other parameters, such as  $n_{e,l}$ ,  $\delta_u$ ,  $\delta_l$ , and  $\kappa$ , do not show a clear relationship with  $\beta_N$  during the suppression phase. These results are consistent with intuitive predictions that the additional  $P_{heat}$  and the lower  $|\delta B_{res}|$  can enhance the plasma performance during the suppression phase.

### 3. Experimental design to achieve $\beta_N$ -enhanced ELM crash suppression

#### 3.1. Experimental conditions favorable to $\beta_N > 2.4$ ELM crash suppression

As shown figures 1 and 4,  $\beta_N$  is below 2.4 in almost all cases of ELM crash suppression. Therefore,  $\beta_N > 2.4$  becomes a goal for plasma performance enhancement during the RMP-driven ELM-crash-suppression phase in KSTAR.

The database analysis results indicate that  $P_{heat}$  and  $I_{RMP}$  are the two main actuators to enhance  $\beta_N$  during the suppression phase. All available NBI sources are used to maximize  $P_{heat}$ . However, only one ECH source of  $\sim 0.6$  MW power is utilized since this power level is optimal for achieving robust ELM crash suppression, considering the ECH effect on the plasma rotation. The ECH injection can change the toroidal rotation profile [50, 51]; in the co- $I_p$  NBI heated discharges of KSTAR, ECH reduces the co- $I_p$  plasma rotation [51]. When the ECH lowers the rotation below the threshold, the ECH-induced rotation drop terminates the suppression phase, as in the DIII-D experiments in which the NBI mix controls the torque affecting the plasma rotation [9]. Additionally,  $P_{heat}$  increases step-by-step to avoid failure in plasma control due to abrupt changes in plasma conditions.  $I_{RMP}$  should be as low as possible but above the suppression threshold level. The  $I_{RMP}$  scan is necessary to obtain the optimal  $I_{RMP}$  level since the  $I_{RMP}$  threshold is sensitive to plasma conditions, such as pressure profile [25], plasm shape [52],  $\beta_N$  [53], RMP configuration [46], etc.

The data distribution in section 2 shows that the  $n = 1$  RMPs obtain higher  $\beta_N$  during the ELM crash suppression than the  $n = 2$  RMPs. Since  $\beta_N \propto 1/I_p$  by definition, the  $n = 1$  RMP-driven suppression at  $q_{95} \sim 5$  suppression window, with lower  $I_p$  as shown in figure 2 ( $I_p \sim 490$ – $540$  kA when  $B_T = 1.8$  T), has an advantageous over  $n = 2$  RMP-driven suppression in  $q_{95} \sim 3.4$ ,  $3.8$ , and  $4.4$  windows ( $I_p \sim 560$ – $800$  kA when  $B_T = 1.8$  T) in achieving higher  $\beta_N$ . Moreover, the  $n =$

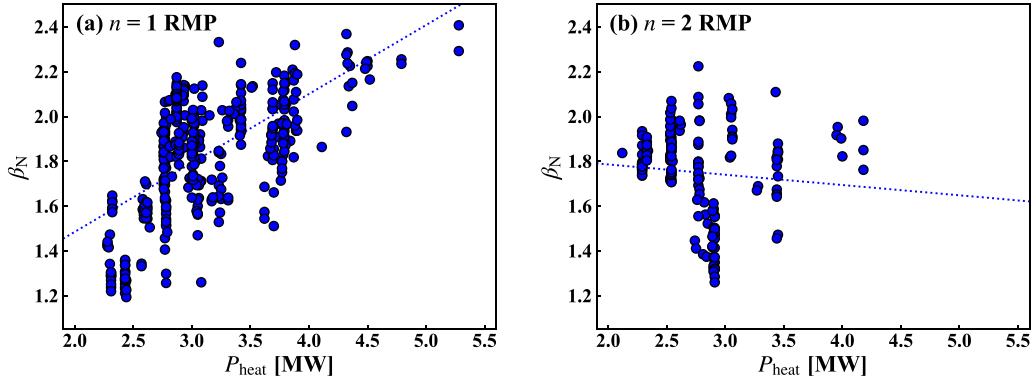


**Figure 1.**  $\beta_N$  in the ELM-crash-suppression phase versus  $P_{\text{heat}}$  in static  $n = 1$  RMP configuration (a) and static  $n = 2$  RMP configuration (b). The dotted straight lines indicate linear regression lines.

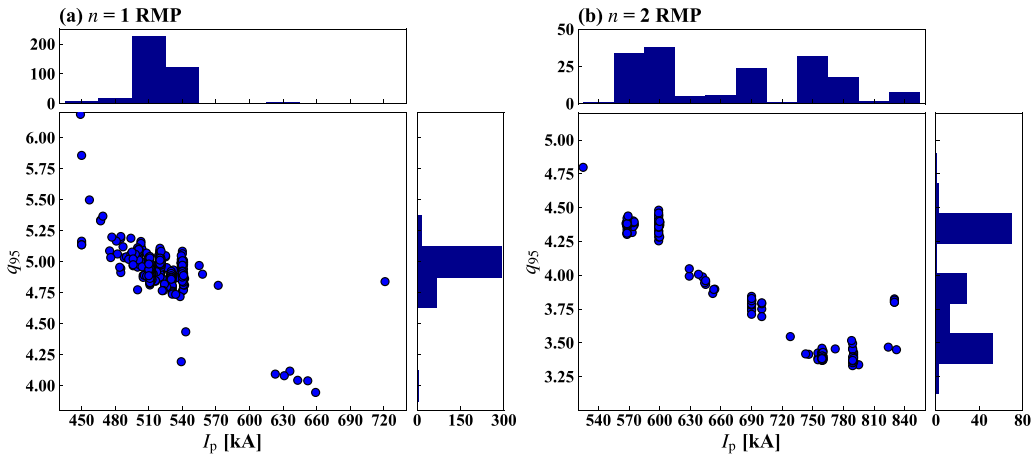


**Figure 2.** Data distributions of ELM crash suppression on  $q_{95}$  (safety factor at 95% of normalized toroidal magnetic flux) and  $I_p$  (plasma current) parameter space with histograms of  $I_p$  (top) and  $q_{95}$  (right): (a) static  $n = 1$  RMP and (b) static  $n = 2$  RMP configurations.

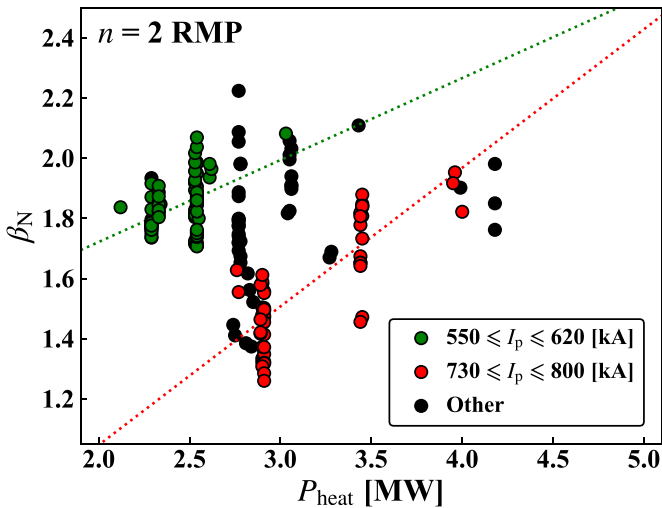


**Figure 3.**  $\beta_N$  versus  $P_{\text{heat}}$  for the  $n = 2$  RMP suppression data sets in two majority  $I_p$  ranges:  $550 \leq I_p \leq 620$  kA (green) and  $730 \leq I_p \leq 800$  kA (red). The ‘Other’ label indicates data outside of these two  $I_p$  ranges. Dotted straight lines represent linear regression lines for each range, with the same color convention.

1 RMP-driven suppression at  $q_{95} \sim 5$  is more reproducible, as evidenced by the number of cases. Therefore, the  $n = 1$  RMP is more effective in achieving  $\beta_N > 2.4$  ELM crash suppression.

This study uses  $\beta_N$  as a metric for evaluating plasma performance to enable prompt comparison, which makes  $n = 1$  RMP of lower  $I_p$  a better option for achieving high  $\beta_N$ . However, it is important to note that the metric should eventually be changed to absolute parameters relevant to the fusion performance.

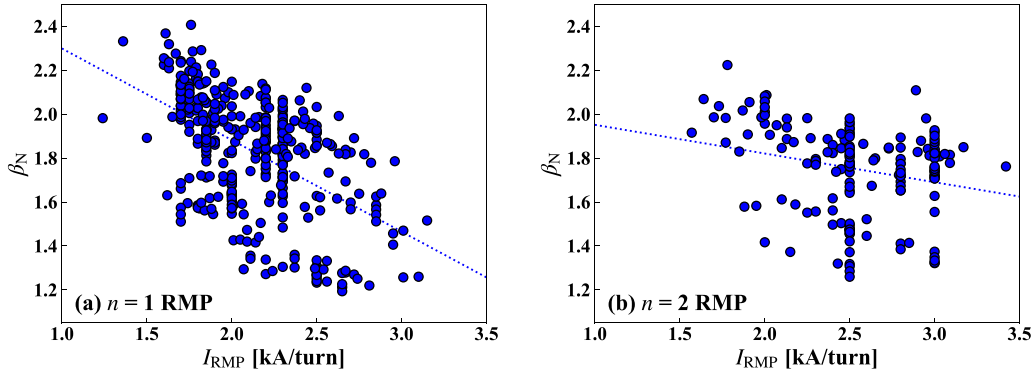
Other conditions, except the major parameters affecting  $\beta_N$ , are set to be highly reproducible to the  $n = 1$  RMP-driven ELM crash suppression:  $B_T = 1.8$  T,  $\delta_{\text{avg}} \sim 0.57$  ( $\delta_u \sim 0.32$  and  $\delta_l \sim 0.82$ ), and  $\kappa \sim 1.72$ .

### 3.2. RMP onset by real-time ML classifier

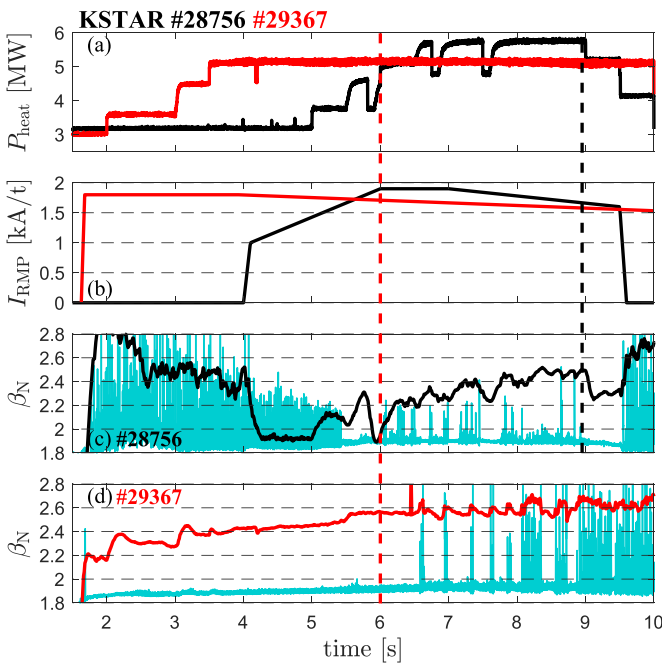
A real-time ML classifier [36], providing the current plasma state, such as L-mode, H-mode, and ELMy phase, is introduced for efficient plasma performance enhancement. The RMP application can be connected to the ML classifier results. For example, by synchronizing the RMP onset timing with the L-H transition timing, the RMP can be fired according to the pre-set  $I_{\text{RMP}}$  target and ramp-up rate before the first ELM crash in the H-mode.

Figure 5 compares experiments for  $\beta_N$  enhancement during the RMP-driven ELM crash suppression in two different RMP triggering methods. Preliminary experiments provide the  $I_{\text{RMP}}$  threshold and determine the optimal heating configuration for





**Figure 4.**  $\beta_N$  in the ELM-crash-suppression phase versus  $I_{RMP}$  in static  $n = 1$  RMP configuration (a) and static  $n = 2$  RMP configuration (b). The dotted straight lines indicate linear regression lines.



**Figure 5.** Comparison of experiments for  $\beta_N$  enhancement during the RMP-driven ELM-crash-suppression phase in KSTAR: RMP onset by conventional pre-set parameters (#28 756, black) and ML classifier (#29 367, red). (a) Total auxiliary heating power. (b) RMP coil current. Time traces of  $\beta_N$  with  $D_\alpha$  (cyan) signal for (c) #28 756 and (d) #29 367.

$\beta_N$  enhancement and stable plasma control. In the case of the conventional pre-set RMP onset (#28 756), the maximum  $P_{heat}$  during the RMP phase is  $\sim 5.76$  MW ( $P_{NBI} \sim 5.3$  MW and  $P_{ECH} \sim 0.45$  MW), as shown in figure 5(a), and  $I_{RMP}$  rises during the H-mode phase according to the pre-set control parameter (figure 5(b)). In the case of the ML-classifier-based RMP onset (#29 367), the maximum  $P_{heat}$  is  $\sim 5.14$  MW ( $P_{NBI} \sim 4.5$  MW and  $P_{ECH} \sim 0.63$  MW), and the  $I_{RMP}$  onset, determined by the ML classifier output, occurs  $\sim 10$  ms after the L–H transition accompanied by the increase in  $\beta_N$  shown in figure 5(d). In the conventional case,  $\beta_N$  increases up to  $\sim 2.47$  under RMP, but the suppression phase appears transiently (figure 5(c)). The ML-based pre-emptive RMP onset

achieves up to  $\beta_N \sim 2.56$  during the stable ELM crash suppression (figure 5(d)) despite  $\sim 11\%$  lower  $P_{heat}$  than the conventional case.  $I_{RMP}$  around the maximum  $\beta_N$  (indicated by vertical dotted lines in figure 5) is similar in the two cases:  $\sim 1.67$  kA/turn in the conventional method (#28 756, 8.95 s) and  $\sim 1.71$  kA  $t^{-1}$  in the ML-based RMP onset (#29 367, 6 s).

The ML-classifier-based RMP onset, originally designed for the pre-emptive ELM crash control, offers an advantage in enhancing  $\beta_N$  compared to the conventional pre-set RMP onset. This  $\beta_N$  enhancement in the pre-emptive RMP onset is primarily due to higher ion temperature in the plasma core region relative to that in the conventional RMP onset [37]. A turbulence and transport analysis in progress will provide a physics understanding of the increased core  $T_i$  in the RMP onset coincident with the L–H transition.

### 3.3. Interactive $I_{RMP}$ control by adaptive feedback RMP ELM controller

In the ML-classifier-based  $\beta_N$  enhancement experiment shown in figure 5,  $I_{RMP}$  gradually decreases to increase  $\beta_N$  under the given  $P_{heat}$ . However, ELM crashes reappear when  $I_{RMP}$  is below  $\sim 1.68$  kA  $t^{-1}$ , and finally, the ELM-crash-suppression phase turns into the ELM-crash-mitigation phase after 8.8 s. Despite the need for an increase in  $I_{RMP}$  to suppress the ELM crash reappearing,  $I_{RMP}$  continues to decrease according to the pre-set  $I_{RMP}$  waveform.

The adaptive feedback RMP ELM controller [15, 38, 39] is introduced to compensate for the limitations of the conventional pre-set  $I_{RMP}$  control through an interactive  $I_{RMP}$  control. The adaptive controller optimizes  $I_{RMP}$  based on a built-in real-time ELM crash frequency monitor. During the suppression phase, the adaptive controller reduces  $I_{RMP}$  to recover plasma confinement, taking into account a hysteresis effect that lowers the  $I_{RMP}$  suppression threshold [15]. If the ELM crash frequency monitor detects ELM crashes during the  $I_{RMP}$  reduction, the controller updates the  $I_{RMP}$  suppression threshold and increases  $I_{RMP}$  until ELM crashes disappear on the ELM crash monitor. Once the suppression phase is restored,  $I_{RMP}$  decreases again. This iterative adjustment of  $I_{RMP}$  can optimize the RMP strength to recover the plasma confinement while maintaining the ELM-crash-suppression

phase. More details about the structure and process of the adaptive feedback algorithm can be found in [38, 39].

The previous KSTAR experiments demonstrate that the adaptive controller can recover the plasma performance up to  $\sim 90\%$  of the non-RMP phase:  $\beta_N$  recovered in the suppression phase is  $\sim 1.91$ , and  $\beta_N$  in the non-RMP phase is  $\sim 2.13$  [15]. Therefore, in this study on  $\beta_N > 2.4$  ELM crash suppression, the adaptive controller is crucial in enhancing the plasma performance during the suppression phase and sustaining the performance-enhanced suppression state. For reference, the  $P_{\text{heat}}$ , discussed in section 3.1, is higher than in the previous experiments proving the performance of the adaptive controller ( $P_{\text{heat}} \sim 3$  MW).

### 3.4. Reduced core resonant magnetic field by ERMP

In order to maximize the  $\beta_N$  enhancement under the given experimental conditions, it is necessary to optimize the RMP spectrum in favor of the plasma confinement, as well as to adjust  $I_{\text{RMP}}$ . The RMP configuration of  $n = 1$ ,  $+90^\circ$  phasing ( $I_{\text{TOP}} = I_{\text{MID}} = I_{\text{BOT}}$  and  $\Delta\phi_{\text{TM}} = \Delta\phi_{\text{MB}} = 90^\circ$ , where  $I_X$  is the RMP coil current of each row and  $\Delta\phi_{XY}$  is the phase difference between rows) has a finite resonant magnetic field strength near the plasma core [31, 40, 42], which can degrade the plasma confinement. The systematic approach by core-null space projection considering RMP coil constraints, such as coil geometry, location, and maximum current, provides the ERMP [40, 41]. The ERMP spectrum has a reduced resonant component in the core region, compared to the conventional  $n = 1$ ,  $+90^\circ$  phasing RMP ( $n = 1$  CRMP) spectrum, while maintaining the edge component above the suppression threshold. The original goal of optimizing RMP spectra for ELM crash control is to avoid disruptive MHD instability driven by core resonant fields, such as locked modes [54]. In this study, it is anticipated that a reduced core component in the ERMP spectrum will enhance the plasma confinement.

## 4. Integrated RMP-based ELM-crash-control process

### 4.1. Experimental validation of the integrated process

The integrated RMP-based ELM-crash-control process incorporates the latest achievements described in section 3, such as the real-time ML classifier, the adaptive feedback RMP ELM controller, and the ERMP spectrum, for efficient  $\beta_N$  enhancement during the ELM-crash-suppression phase. The integrated process unfolds as follows: first, the ERMP spectrum is triggered based on real-time ML classifier output. Next, the control authority of the ML classifier is transferred to the adaptive controller. Finally, the adaptive controller optimizes  $I_{\text{RMP}}$  to achieve enhanced  $\beta_N$  during the suppression phase.

The performance of the integrated process is validated by comparing  $\beta_N$  during the suppression phase in different  $I_{\text{RMP}}$  control methods and  $n = 1$  RMP spectra (figure 6). The comparisons include 1)  $n = 1$  CRMP with a constant  $I_{\text{RMP}}$  of

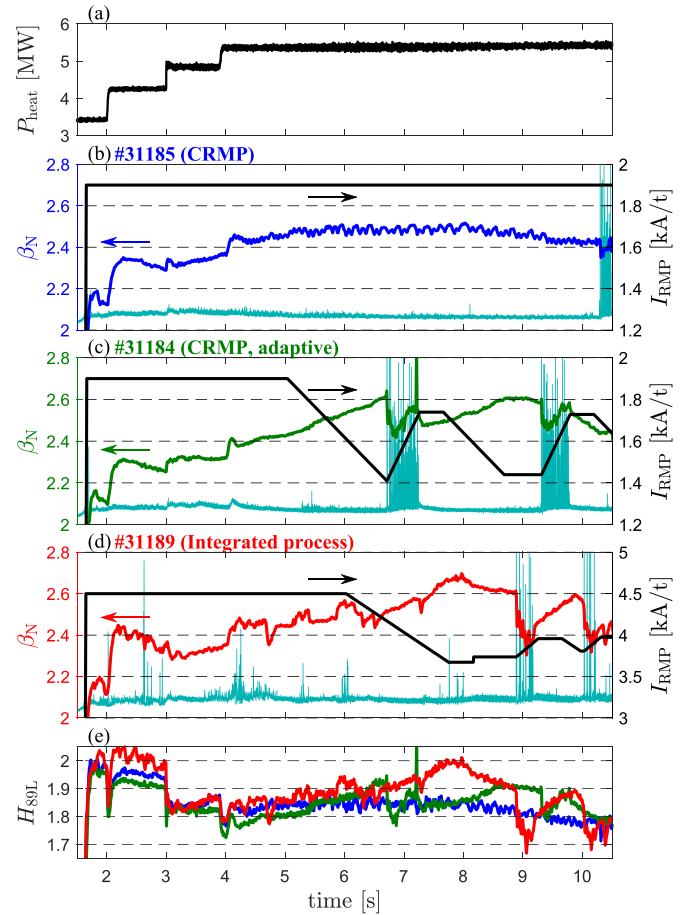


**Figure 6.** Comparison of  $\beta_N$  during the  $n = 1$  RMP-driven ELM crash control. (a) Total auxiliary heating power. Time traces of  $\beta_N$ ,  $D_\alpha$  (cyan), and RMP coil current (black) in (b) the CRMP with pre-set constant  $I_{\text{RMP}}$  (#31 185), (c) the CRMP with adaptive feedback control (#31 184), and (d) the ERMP with adaptive feedback control (#31 189). (e) H-factor. In (b)–(d),  $I_{\text{RMP}}$  is the top coil current among three-row RMP coils (TOP, MIDDLE, and BOTtom) in KSTAR. In CRMP,  $I_{\text{TOP}} = I_{\text{MID}} = I_{\text{BOT}}$ , while in ERMP,  $I_{\text{TOP}} = I_{\text{BOT}} > I_{\text{MID}}$ .

$1.9 \text{ kA t}^{-1}$  (#31 185), 2)  $n = 1$  CRMP with adaptive  $I_{\text{RMP}}$  control (#31 184), and 3)  $n = 1$  ERMP with adaptive  $I_{\text{RMP}}$  control (integrated process, #31 189). In all cases, the RMP onset timing is when the real-time ML classifier indicates the L–H transition. During the RMP phase,  $B_T = 1.8 \text{ T}$ ,  $\delta_{\text{avg}} \sim 0.57$ ,  $\kappa \sim 1.72$ ,  $I_p \sim 490 \text{ kA}$ , and  $q_{95} \sim 5.1$ . As shown in figure 6(a),  $P_{\text{heat}}$  increases step-by-step to avoid failure in plasma control, and the maximum  $P_{\text{heat}}$  is  $\sim 5.4 \text{ MW}$  ( $P_{\text{NBI}} \sim 4.8 \text{ MW}$  and  $P_{\text{ECH}} \sim 0.58 \text{ MW}$ ). Figures 6(b)–(d) show that  $I_{\text{RMP}}$ , representing the top coil current among three-row RMP coils, in the ERMP spectrum is consistently larger than the CRMP spectrum throughout the discharge. However, in the ERMP spectrum, the top and bottom coil currents are  $\sim 23.8$  times larger than the mid coil current (i.e.  $I_{\text{TOP}} = I_{\text{BOT}} \sim 23.8 I_{\text{MID}}$ ), resulting in a resonant magnetic field lower than expected from the  $I_{\text{RMP}}$  alone. The Ideal Perturbed Equilibrium Code (IPEC) [55] calculations, shown in figure 7, indicate that the ERMP spectrum (red line) applied in the integrated process produces  $\sim 14\%$  lower  $|\delta B_{\text{res}}|$  near the core region ( $\psi_N \sim 0.48$ ) than

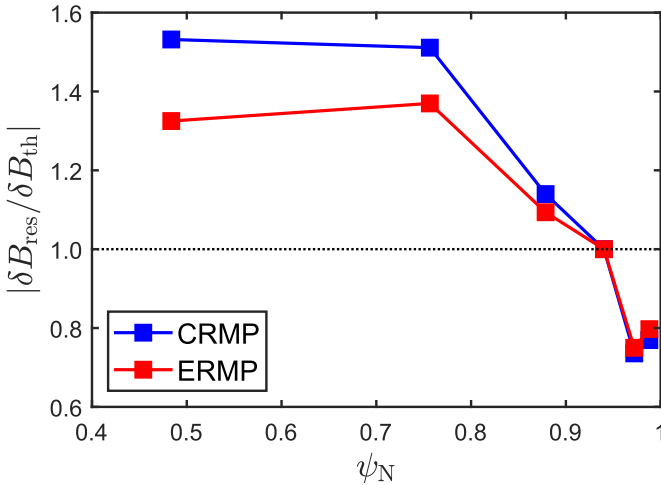


**Figure 7.** Comparison of resonant magnetic field ( $\delta B_{\text{res}}$ ) spectra. CRMP is the conventional  $n = 1$ ,  $+90^\circ$  phasing RMP applied in #31 184 and #31 185. ERMP is the  $n = 1$  edge-localized RMP for #31 189.

CRMP (blue line) when  $|\delta B_{\text{res}}|$  around the pedestal top ( $\psi_N \sim 0.94$ ) is the suppression threshold, based on the assumption that the suppression threshold is similar across different RMP spectra [46].

One technical challenge in combining the ML classifier and the adaptive controller is ensuring a smooth transition of  $I_{\text{RMP}}$  control authority. In both discharges (#31 184 and #31 189), where the adaptive feedback control algorithm is activated 3 s and 4 s after the RMP onset, respectively, the adaptive controller takes over  $I_{\text{RMP}}$  control authority from the ML classifier without any issues. For reference, the pre-set parameters for adaptive control are as follows: the  $I_{\text{RMP}}$  ramp-up rate is  $0.6 \text{ kA t}^{-1} \text{ s}^{-1}$ , the ramp-down rate is  $0.3 \text{ kA t}^{-1} \text{ s}^{-1}$  in #31 184 and  $0.5 \text{ kA t}^{-1} \text{ s}^{-1}$  in #31 189, and the waiting time for  $I_{\text{RMP}}$  adjustment after the restoration of the suppression phase is 400 ms.

In the reference case ( $n = 1$  CRMP with constant  $I_{\text{RMP}}$ , i.e. #31 185), the maximum  $\beta_N$  during the suppression phase is  $\sim 2.49$  (figure 6(b)). Compared to the previous ML-classifier-based RMP onset case (#29 367 in figure 5), the maximum  $\beta_N$  is  $\sim 3\%$  lower despite  $\sim 5\%$  higher  $P_{\text{heat}}$ . About 11% higher  $I_{\text{RMP}}$  in #31 185 ( $1.9 \text{ kA t}^{-1}$ ) could be the main reason for the lower  $\beta_N$ , but it contributes to the stable  $\beta_N > 2.4$  suppression phase lasting over 6 s ( $\sim 2.8$  s duration in #29 367).

In #31 184 (figure 6(c)), the adaptive controller reduces  $I_{\text{RMP}}$  three times to enhance the plasma performance. At the first attempt,  $\beta_N$  increases up to  $\sim 2.61$  ( $I_{\text{RMP}} \sim 1.43 \text{ kA t}^{-1}$ ), but ELM crashes reappear soon. The adaptive controller restores the suppression phase in  $\sim 0.55$  s by increasing  $I_{\text{RMP}}$  to  $\sim 1.74 \text{ kA t}^{-1}$ . The second attempt starts after the pre-set waiting time of 400 ms following the recovery of the suppression phase. The reduction in  $I_{\text{RMP}}$  during the second attempt stops at  $I_{\text{RMP}} \sim 1.44 \text{ kA t}^{-1}$ , which corresponds to the lower limit of  $I_{\text{RMP}}$  determined by the adaptive controller based on the results of the first attempt.  $\beta_N \sim 2.6$  suppression phase is maintained for  $\sim 0.6$  s, a longer duration than the first attempt, and then

the suppression phase transits to the ELM-crash-mitigation phase. The controller achieves the suppression phase recovery in  $\sim 0.48$  s by increasing  $I_{\text{RMP}}$  to  $\sim 1.73 \text{ kA t}^{-1}$ , similar to the first recovery. During the last attempt, the  $I_p$  flat-top ends at 10.5 s.

In the integrated process (#31 189, figure 6(d)), the ERMP spectrum is applied instead of the CRMP spectrum in the previous two cases. The adaptive control with ERMP (i.e. integrated process) achieves a higher  $\beta_N$  than the adaptive control with CRMP. During the RMP phase, the maximum  $\beta_N$  is  $\sim 2.69$  around 7.9 s, but sparse ELM crashes appear then. The maximum  $\beta_N$  of the stable suppression phase is  $\sim 2.65$  around 8.1 s ( $\sim 2.61$  in #31 184). The duration of  $\beta_N > 2.6$  suppression is  $\sim 1.4$  s,  $\sim 2.3$  times longer than the adaptive control with CRMP. Moreover, the suppression in  $\beta_N$  above 2.4 (the lower limit of target  $\beta_N$ ) is sustained for  $\sim 4$  s ( $\sim 60\tau_E$ ), while the duration of  $\beta_N > 2.4$  suppression is  $\sim 2.1$  s ( $\sim 31\tau_E$ ) in #31 184. Like #31 184, the mitigation phase follows the  $\beta_N \sim 2.6$  suppression phase. The  $\beta_N$  drop in the mitigation phase is about two times larger than observed in the CRMP (#31 184). However, the restoration time for the suppression phase ( $\sim 0.30$  s and  $\sim 0.21$  s) is  $\sim 38\% - 62\%$  shorter than that of #31 184 ( $\sim 0.55$  s and  $\sim 0.48$  s). The shorter restoration time means that a smaller change in  $I_{\text{RMP}}$  is sufficient to recover the suppression since the pre-set  $I_{\text{RMP}}$  ramp-up rate for the adaptive control is  $0.6 \text{ kA t}^{-1} \text{ s}^{-1}$  for both ERMP and CRMP cases. Similarly, the recovery time for  $\beta_N \sim 2.6$  suppression ( $\sim 0.70$  s) is  $\sim 51\%$  shorter than #31 184 ( $\sim 1.43$  s). The reduced  $|\delta B_{\text{res}}|$  inside the edge region in the ERMP is the most likely reason for the quicker  $\beta_N$  recovery.

In two adaptive control cases (#31 184 and #31 189), the pattern of  $I_{\text{RMP}}$  change is consistent with the  $I_{\text{RMP}}$  optimization process described in section 3.3, except for one case that requires explanation. In the integrated process (#31 189), the adaptive controller halts the decrease in  $I_{\text{RMP}}$  at  $\sim 7.76$  s when an ELM crash occurs. However, these sporadic ELM crashes do not trigger the mitigation phase. Consequently, the adaptive controller suspends the decision of  $I_{\text{RMP}}$  ramp-up, in contrast to the immediate  $I_{\text{RMP}}$  ramp-up responding to the mitigation phase (for example,  $\sim 8.9$  s in #31 189). After a delay of  $\sim 400$  ms, the controller triggers a jump in  $I_{\text{RMP}}$  of  $\sim 0.06 \text{ kA t}^{-1}$  (determined by the internal process) at  $\sim 8.17$  s to achieve stable suppression and maintains  $I_{\text{RMP}}$  as the updated lower limit of  $I_{\text{RMP}}$ . This increase in  $I_{\text{RMP}}$  can reinforce the reduction of  $\beta_N$  after the  $\beta_N$  peak at  $\sim 7.9$  s.

In conclusion, the integrated RMP-based ELM-crash-control process sets a new record for  $\beta_N$  during the RMP-driven ELM crash suppression in KSTAR, reaching  $\beta_N \sim 2.65$ . The adaptive feedback control algorithm achieves higher  $\beta_N$  during the suppression [ $\beta_{N,\text{max}} \sim 2.65$  in the ERMP spectrum (i.e. integrated process) and  $\beta_{N,\text{max}} \sim 2.61$  in the CRMP spectrum] than the conventional pre-set  $I_{\text{RMP}}$  operations ( $\beta_{N,\text{max}} \sim 2.49$  in #31 185). The attempts to achieve  $\beta_N$  above the target value of 2.4 during the suppression phase extend the accessible range of the suppression in KSTAR to  $\beta_N > 2.4$  regions. The H-factor ( $H_{99L} = \tau_{E,\text{exp}}/\tau_{E,99L}$ , where  $\tau_{E,\text{exp}}$  is the energy confinement time from experiments and  $\tau_{E,99L}$  is the energy

confinement time derived from a multi-machine scaling [56]) confirms the plasma confinement enhancement (figure 6(e)). In this analysis, the injected  $P_{\text{heat}}$  is used to calculate  $\tau_{E,89L}$ . In #31 189 (integrated process) and #31 184 (CRMP with adaptive control),  $H_{89L}$  increases up to  $\sim 1.99$  and  $\sim 1.92$ , respectively, coincident with the timing of maximum  $\beta_N$ . In the reference case (#31 185), the maximum  $H_{89L}$  at  $P_{\text{heat}} \sim 5.4$  MW is  $\sim 1.84$ .

$\beta_N \geq 2.6$  ELM crash suppression is comparable to the target  $\beta_N$  of the EU DEMO1 design option ( $\beta_N = 2.6$  [34]) but 5%–7% lower than the target of the K-DEMO first phase ( $\beta_N = 2.8$  [33]). Compared to the DIII-D (similar size to KSTAR)  $\beta_N$  record dataset of RMP-driven ELM crash suppression ( $\beta_N \sim 2.5$ ,  $P_{\text{heat}} > 7$  MW,  $I_p \sim 1.2$  MA [32]), KSTAR achieves higher  $\beta_N$  during the suppression phase with lower  $P_{\text{heat}}$  ( $\sim 5.4$  MW). However, in this comparison, the relatively low  $I_p$  in the KSTAR  $\beta_N \sim 2.65$  case ( $I_p \sim 0.49$  MA) is favorable for obtaining higher  $\beta_N$  than the DIII-D  $\beta_N$  record. As mentioned in section 3.1,  $\beta_N$  is an insufficient metric to describe the absolute plasma performance. For example, the  $I_p a B_T$  product is a simple metric for fusion performance [57]. While  $I_p a B_T \sim 1.05$  in the DIII-D  $\beta_N$  record [32], in the KSTAR case,  $I_p a B_T \sim 0.41$  (with a minor radius of  $a \sim 0.46$  m) despite its higher  $\beta_N$ . This study that enhances the plasma performance during the suppression phase will be extended to increase the absolute plasma performance by introducing a metric relevant to the fusion performance.

#### 4.2. $\beta_N$ recovery after the mitigation phase onset

During the adaptive control in both the ERMP and the CRMP cases, the mitigation phase, accompanied by  $\beta_N$  drop, occurs after the  $\beta_N \sim 2.6$  suppression phase (figures 6(c) and (d)). This section investigates the  $\beta_N$  recovery after the onset of the mitigation phase. It is worth noting that other MHD instabilities are unlikely to contribute to the rapid  $\beta_N$  reduction observed in the mitigation phases since there are no measurable instability events during the RMP phase except the mitigated ELM crashes.

Figure 8 shows the relative change in the parameters of interest compared to their value at the onset of the mitigation phase. The relative change of variable  $F$  can be written by  $\Delta F(t_m) = (F(t) - F(t_m))/F(t_m)$ , where  $t_m$  denotes the time of the mitigation phase onset. To focus on the temporal change of  $\Delta F(t_m)$ , time-averaged values for  $n_{e,l}$  (from TCI) and  $T_e$  [from electron cyclotron emission (ECE) radiometry [58]] are obtained for each 10 ms time window. The relative change in  $\beta_N$  ( $\Delta\beta(t_m)$ , figure 8(b)) exhibits a similar pattern to  $\Delta T_e(t_m)$  on  $\psi_N \sim 0.2$  (figure 8(c)) and  $\psi_N \sim 0.8$  (figure 8(d)). The evolution of  $T_e$  spans a wide radial range, and  $\Delta T_e(t_m)$  has a similar level with  $\Delta\beta(t_m)$ , except for changes supposed to be attributed to the mitigated ELM crashes. The similarity between  $\Delta\beta(t_m)$  and  $\Delta T_e(t_m)$  increases as close to the plasma core. The relationship between  $\Delta\beta(t_m)$  and  $\Delta n_{e,l}(t_m)$  is not as obvious as the relationship between  $\beta_N$  and  $T_e$  (figure 8(e)). The above observations indicate that  $T_e$  predominantly influences the drop or recovery of  $\beta_N$ .

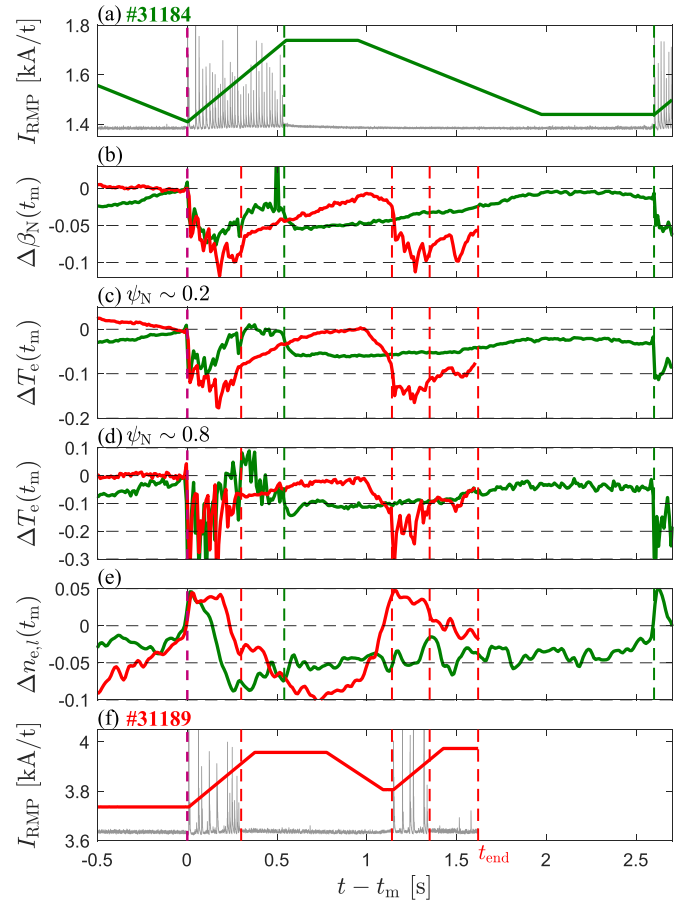


**Figure 8.** Comparison of the time evolution in electron density and temperature. (a) RMP coil current (green) and  $D_\alpha$  signal (grey) in #31 184 (CRMP spectrum with adaptive control). The relative change to the value at the onset of the mitigation phase: (b)  $\beta_N$ , (c) electron temperature ( $T_e$ ) on  $\psi_N \sim 0.2$ , (d)  $T_e$  on  $\psi_N \sim 0.8$ , and (e) line-averaged electron density. (f)  $I_{\text{RMP}}$  (red) and  $D_\alpha$  (grey) in #31 189 (integrated process). In (b)–(e), green corresponds to #31 184, and red does #31 189. Vertical dotted lines indicate the onset and end of the mitigation phase in #31 184 and #31 189 and the end of the  $I_p$  flat-top in #31 189.  $t_m$  and  $t_{\text{end}}$  denote the time of the mitigation phase onset and the end of the  $I_p$  flat-top, respectively.

An interesting observation regarding  $\Delta n_{e,l}(t_m)$  is that  $\Delta n_{e,l}(t_m)$  becomes larger than zero at the onset of the mitigation phase in both the ERMP and the CRMP cases. During the suppression phase,  $\Delta n_{e,l}(t_m) < 0$ . This behavior is similar to the suppression threshold in electron density observed in DIII-D [9] and ASDEX upgrade [11]. The electron density on the pedestal top ( $n_{e,\text{ped}}$ ) at the onset of the mitigation phase (in #31 184,  $n_{e,\text{ped}} \sim 2.71 \times 10^{19}$  and  $\sim 2.57 \times 10^{19} \text{ m}^{-3}$ , while in #31 189,  $n_{e,\text{ped}} \sim 2.65 \times 10^{19}$  and  $\sim 2.69 \times 10^{19} \text{ m}^{-3}$ ) is higher than the maximum  $n_{e,\text{ped}}$  observed during the suppression phase so far in KSTAR ( $\sim 2.5 \times 10^{19} \text{ m}^{-3}$  [14]). However, further exploration of the high  $n_{e,\text{ped}}$  region is necessary to confirm the density threshold in the KSTAR [14].

The increase in  $\beta_N$  independent of the change in  $I_{\text{RMP}}$  is observed in both the ERMP and CRMP cases. During the  $I_{\text{RMP}}$  ramp-up to restore the ELM crash suppression,  $\beta_N$  is recovered by  $\sim 4.3\%$  in the ERMP case ( $t - t_m \sim 0.26$ – $0.38$  s)



and  $\sim 5.4\%$  in the CRMP case ( $t - t_m \sim 0.11\text{--}0.46$  s). During the constant  $I_{RMP}$  due to the waiting time in the adaptive control,  $\beta_N$  increases by  $\sim 3.4\%$  in the ERMP case ( $t - t_m \sim 0.38\text{--}0.78$  s) and  $\sim 1\%$  in the CRMP case ( $t - t_m \sim 0.6\text{--}0.95$  s). The plausible explanation for this  $\beta_N$  recovery, not influenced by  $I_{RMP}$ , is that the plasma can naturally restore  $\beta_N$  to a certain extent without relying on a decrease in  $I_{RMP}$  if the mitigated ELM crashes excessively degrade  $\beta_N$  below the level anticipated by the RMP strength and auxiliary heating power. For example, in the ERMP case, during the period of constant  $I_{RMP}$  ( $\sim 3.96 \text{ kA t}^{-1}$ ),  $\beta_N$  increases from  $\sim 2.46$  ( $t - t_m \sim 0.38$  s, or  $t \sim 9.26$  s) to  $\sim 2.55$  ( $t - t_m \sim 0.78$  s, or  $t \sim 9.66$  s). Considering that  $\beta_N \sim 2.58$  at  $t \sim 7.16$  s under similar  $I_{RMP}$  and  $P_{\text{heat}}$  conditions (figure 6(d)), it suggests that the plasma at  $t - t_m \sim 0.38$  s has the potential to recover  $\beta_N$ . In the CRMP case, the restoration of the suppression phase leads to a transient drop in  $\beta_N$ . This  $\beta_N$  drop can be attributed to the higher  $\beta_N$  ( $\beta_N \sim 2.53$  at  $I_{RMP} \sim 1.73 \text{ kA t}^{-1}$ ) just before the suppression restoration ( $t - t_m \sim 0.54$  s) than  $\beta_N \sim 2.5$  under similar  $I_{RMP}$  and  $P_{\text{heat}}$  conditions in the previous time ( $t \sim 5.61$  s, figure 6(c)). However, in this  $\beta_N$  drop of the CRMP case, further investigation is required to explain the overshoot in  $\beta_N$  recovery and the sustainment of higher  $\beta_N$  levels during the mitigation phase.

During the  $I_{RMP}$  ramp-down after the waiting time in the adaptive control, the evident acceleration in  $\beta_N$  recovery is observed in the CRMP case, whereas it is unclear in the ERMP case. This absence of accelerated  $\beta_N$  recovery in the ERMP can be attributed to the quick restoration of the suppression phase. In the ERMP, during the  $I_{RMP}$  ramp-up to restore the suppression phase,  $I_{RMP}$  increases by  $\sim 5.8\%$ , while  $\sim 21\%$  in the CRMP. Furthermore, at the end of the waiting time ( $t - t_m \sim 0.78$  s),  $\beta_N$  reaches  $\sim 98\%$  of the value at the onset of the mitigation phase and  $\sim 97\%$  of the maximum  $\beta_N$  during the stable suppression phase. In the ERMP, the impact of change in  $|\delta B_{\text{res}}|$  on  $\beta_N$  cannot be as significant as in the CRMP.

Figure 9 shows the repetition frequency of ELM crashes ( $f_{\text{rep}}$ ) during the mitigation phase. In the CRMP case (figures 9(a) and (b)), the onset of  $\beta_N$  recovery (indicated by black dotted lines) occurs  $\sim 30$  ms before the increase in  $f_{\text{rep}}$  to above  $\sim 60$  Hz (indicated by magenta dotted lines), while in the ERMP case (figures 9(c) and (d)), it occurs  $\sim 20$  ms after. Since the stored energy loss driven by ELM crash becomes lower in a higher  $f_{\text{rep}}$  [59], a higher  $f_{\text{rep}}$  can cause the recovery of  $\beta_N$ . However, further investigation is required to clarify the causality between the onset of  $\beta_N$  recovery and the increase in  $f_{\text{rep}}$ , and figure out the  $f_{\text{rep}}$  threshold for  $\beta_N$  recovery if  $f_{\text{rep}}$  is related to  $\beta_N$  recovery. A comprehensive simulation can address this matter, but such an investigation is beyond the scope of this paper.

#### 4.3. Turbulent fluctuation in the suppression phase of ERMP and CRMP spectra

The KSTAR Electron Cyclotron Emission Imaging (ECEI) system [60] is introduced to analyze turbulent fluctuations in the ERMP and CRMP discharges. Among 24 (vertical)  $\times$  8

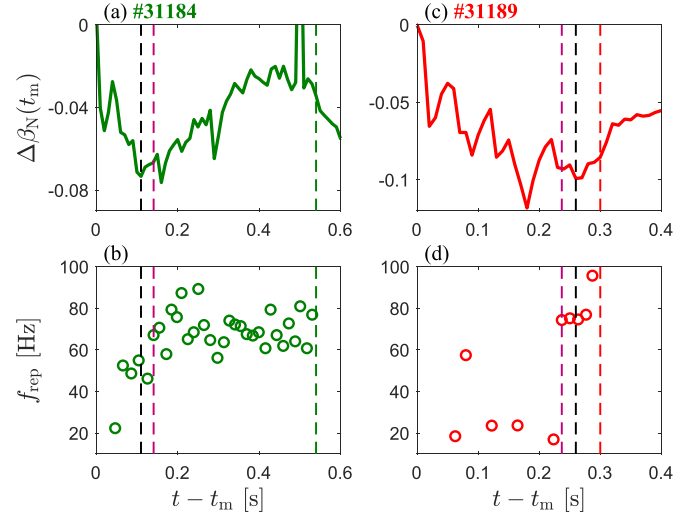


**Figure 9.** The relative change of  $\beta_N$  to its value at the onset of the mitigation phase in #31 184 (CRMP) (a) and in #31 189 (ERMP) (c). The repetition frequency of ELM crash in #31 184 (CRMP) (b) and in #31 189 (ERMP) (d). Black dotted line: the onset time of  $\beta_N$  recovery. Magenta: the time of the  $f_{\text{rep}}$  increase to above  $\sim 60$  Hz. Green (#31 184) and red (#31 189): the end time of the mitigation phase.

(radial) ECEI channels in a two-dimensional space on the poloidal cross-section, the vertically adjacent two channels are employed to obtain the coherence ( $\gamma_{xy}(f)$ ) spectrum and the relative fluctuation of electron temperature ( $\tilde{T}_e/T_e$ ) through correlation analysis.  $\tilde{T}_e/T_e$  can be derived from the relation  $\tilde{T}_e/T_e = \sqrt{2B_{\text{vid}}C_{xy}(0)/B_{\text{IF}}}$  [61], where  $B_{\text{vid}}$  is the video bandwidth (300 kHz for ECEI),  $B_{\text{IF}}$  is the Intermediate Frequency (IF) bandwidth (700 MHz for ECEI),  $C_{xy}(0)$  is the cross-correlation coefficient at zero lag time. However, the ECEI view windows only cover the Low Field Side (LFS) edge in #31 184 (CRMP) and #31 189 (ERMP). For analyzing fluctuations inside the edge of the plasma, the ECE radiometry is utilized. The ECE radiometry channels are distributed radially along the mid-plane, but the distance between adjacent channels is not sufficiently close for correlation analysis. Alternatively, the standard deviation ( $\sigma$ ) of  $T_e$  for a specific time period represents the fluctuation level during that period. Total  $T_e$  can be expressed as  $T_e = T_{e,0} + \tilde{T}_e$ , where  $T_{e,0}$  and  $\tilde{T}_e$  represent the steady and fluctuation part of electron temperature, respectively. Based on the assumption that  $\langle T_e \rangle \sim T_{e,0}$  ( $\langle T_e \rangle$  denotes the time-averaged  $T_e$ ) within the time window of interest,  $\sigma(T_e)$  can be a reliable proxy for quantifying the magnitude of fluctuations, since  $\sigma(T_e)$  is the square root of the expected value of  $(T_e - \langle T_e \rangle)^2$ .

Figure 10 shows fluctuation levels of the electron temperature in different radial positions. The ECEI analysis calculates  $\gamma_{xy}(f)$  and  $C_{xy}(0)$  in non-overlapping 50 ms time segments. Within this time segment, the sensitivity of  $\tilde{T}_e/T_e$ , determined by  $\tilde{T}_e^2/T_e^2 \geq 2B_{\text{vid}}/\sqrt{NB_{\text{IF}}}$  [62], is  $\sim 0.2\%$ , where the independent sample number ( $N$ ) is 25 000 at a 500 kHz sampling rate of ECEI. The ECE analysis obtains  $\sigma(T_e)$  for each non-overlapping 50 ms time window, corresponding to the time segment length used in ECEI analysis. In the time of

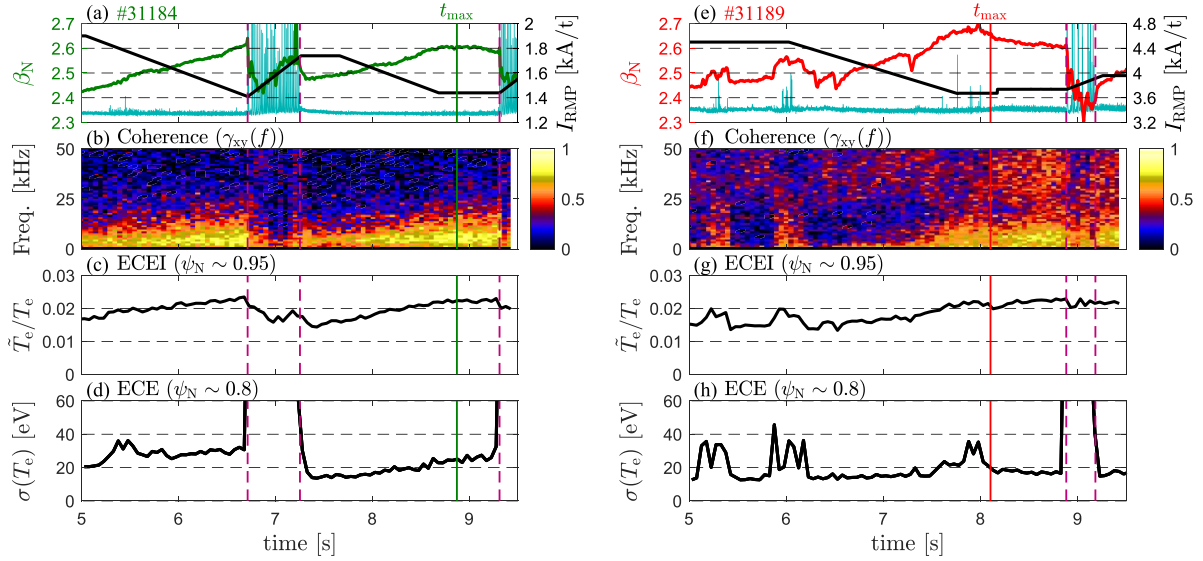


**Figure 10.** Comparison of electron temperature fluctuation. (a) and (e): Time traces of  $\beta_N$ ,  $D_\alpha$  (cyan), and RMP coil current (black). (b) and (f): Coherence spectra from two vertically adjacent ECEI channels on low-field side mid-plane ( $\psi_N \sim 0.95$ ). (c) and (g): Relative fluctuation level measured by ECEI channels on  $\psi_N \sim 0.95$ . (d) and (h): Standard deviation of  $T_e$  from the ECE radiometry channel on  $\psi_N \sim 0.8$ . (a)–(d) for #31 184 (adaptive control with  $n = 1$  CRMP spectrum) and (e)–(h) for #31 189 (integrated process). The maximum  $\beta_N$  at the stable suppression is indicated by  $t_{\max}$ .

interest,  $\sigma(T_e)/\sigma(T_N) > 2.9$ , where  $T_N$  is the thermal noise temperature of the system. For reference, the sampling rate of ECE radiometry is 500 kHz in the discharge of interest. The resonant positions of ECE and ECEI channels are determined by considering the poloidal magnetic field and relativistic broadening [63]. Due to the potential decrease in correlation analysis accuracy and the possibility of overestimating  $\sigma(T_e)$  caused by the frequent ELM crashes, the discussion on fluctuation level does not focus on the period of the ELM-crash-mitigation phase, indicated by magenta dotted lines.

The ERMP and the CRMP exhibit a similar trend in turbulent fluctuations on the plasma edge ( $\psi_N \sim 0.95$ ) during the suppression phase since the ERMP is designed to have the same  $\delta B_{\text{res}}$  spectrum as the CRMP at the plasma edge. In both suppression phases under the ERMP and CRMP spectra, as  $I_{\text{RMP}}$  decreases (or  $\beta_N$  increases), the coherence spectra on  $\psi_N \sim 0.95$  get broadened,  $\gamma_{xy}(f)$  increases in the frequency range  $f < 25$  kHz (figures 10(b) and (f)), and the relative fluctuation level ( $\tilde{T}_e/T_e$ ) at the plasma edge increases (figures 10(c) and (g)). This trend is more evident in the CRMP case. In the ERMP, during the period when  $\beta_N$  decrease by  $\sim 2\%$  after reaching the maximum  $\beta_N$  of the stable suppression phase (indicated by the vertical line labeled  $t_{\max}$ ),  $\tilde{T}_e/T_e$  slightly increases and  $\gamma_{xy}(f)$  in  $f > 25$  kHz becomes strong. When  $I_{\text{RMP}}$  decreases, the reduction in  $|\delta B_{\text{res}}|$  can weaken the RMP-induced classical quasi-linear transport [25, 64] or stabilize turbulent fluctuations driven by the anisotropic  $E \times B$  shearing rate in a magnetic island [65]. However, the expected gradient steepening due to the  $\beta_N$  enhancement, associated with reducing the quasi-linear transport coefficient or the RMP-driven turbulence, can linearly drive additional turbulent

fluctuations. Thus, it follows that the observed increase in turbulent fluctuations might be originated from the linear drive of turbulence fluctuations due to the gradually enhanced pedestal with the decrease in RMP strength, which suggests that on the plasma edge in the present experiments, the driving mechanism is more dominant than the turbulence stabilization mechanism when  $I_{\text{RMP}}$  decreases. On the other hand, further analysis is required to tell whether the elevated fluctuation level is related to the onset of the mitigation phase.

In the CRMP case, the fluctuation level ( $\sigma(T_e)$ ) increases in the region of  $\psi_N \sim 0.8$  as  $I_{\text{RMP}}$  decreases (or  $\beta_N$  increases) if disregarding bumps that coincide with sporadic bursts of the  $D_\alpha$  signal around 5.4 s (figure 10(d)). On the other hand, in the ERMP, there are no significant changes in the fluctuation level, except for fluctuations driven by sporadic ELM crashes (figure 10(h)). Supposing that the observed fluctuation level on  $\psi_N \sim 0.8$  is governed by the same mechanism as the plasma edge explained above, the impact of  $I_{\text{RMP}}$  on the magnitude of the relevant turbulence on  $\psi_N \sim 0.8$  may be insignificant in the ERMP. This can be attributed to a smaller magnitude of  $|\delta B_{\text{res}}|$  on  $\psi_N \sim 0.8$  in the ERMP compared to the CRMP, as shown in figure 7, which implies that the applied  $\delta B_{\text{res}}$  in the ERMP may not penetrate into the resonant surface near  $\psi_N \sim 0.8$ . It is well-known that only when the applied resonant field penetrates into the resonant surface, the ambient magnetic topologies can be reorganized. Consequently, this change in the magnetic topology can increase particle or heat transport, affecting instability/fluctuation. Thus, the comparison of the fluctuation level on  $\psi_N \sim 0.8$  suggests that the ERMP spectrum affects the radially narrower regions localized to the plasma edge, compared to the CRMP spectrum.

## 5. Plans for expanding the integrated process to long-pulse ELM-less operation

This section explores the expansion of the integrated RMP-based ELM-crash-control process, excluding the matter of a metric for evaluating plasma performance. The integrated process needs to consider issues related to long pulse and ELM-less operation for further improvement, although it already demonstrates the ability to enhance plasma performance during the ELM-crash-suppression phase.

Figure 6(d) shows that the integrated process does allow for the reappearance of ELM crashes when enhancing  $\beta_N$  in the suppression phase. While enhancing the plasma performance in the ELM-crash-suppression plasmas, it is crucial to avoid any single ELM crash, which can threaten machine safety in ITER and future fusion devices. The latest version of the adaptive feedback RMP ELM controller incorporates a real-time detector for a precursor to ELM-crash-suppression loss [39], which can pre-emptively control  $I_{RMP}$  to prevent the ending of the suppression phase. By integrating this update, the integrated process can move closer to achieving the plasma performance-enhanced RMP-based ELM-less operation. However, before deployment, the precursor detector should be optimized for experimental conditions favorable to the plasma performance enhancement.

KSTAR, equipped with superconducting magnets, is an ideal testbed for expanding the integrated process to the long-pulse ELM-less operation. To consider the long-pulse issue, the integrated process can incorporate any long-pulse-relevant actuators compatible with the plasma performance-enhanced RMP-driven ELM crash suppression, even if they are unrelated to the RMP technique. One of the potential candidates is the KSTAR divertor plasma detachment control based on the simplified real-time modeling [66], reducing the heat load on PFCs. However, the impurity seeding, the primary actuator of the detachment control, has a side effect on core plasma performance [67] and affects conditions to access ELM crash suppression by changing electron density and recycling conditions [68, 69]. Therefore, incorporating the detachment control requires upgrading the integrated process to balance plasma detachment, ELM crash suppression, and plasma performance enhancement.

## 6. Summary

The RMP technique is a promising method to control the ELM crash. However, the RMP-driven ELM crash control is accompanied by an unwanted degradation in plasma performance. Based on the reliability of the RMP-driven ELM crash suppression in KSTAR, the database for KSTAR RMP-driven ELM-crash-control experiments is constructed to investigate the plasma performance during the ELM-crash-suppression phase and identify experimental conditions favorable to  $\beta_N$  enhancement. In this database,  $\beta_N$  is a metric for the plasma confinement performance. Among the 283 discharges

included in the database, the data sets from 169 ELM-crash-suppression discharges indicate that 1) the auxiliary heating power ( $P_{heat}$ ) and the RMP coil current ( $I_{RMP}$ ) are the two main parameters influencing  $\beta_N$  during the suppression phase, 2) in KSTAR, the lower  $I_p$  conditions for the  $n = 1$  RMP suppression have an advantage over the  $n = 2$  RMP suppression in achieving higher  $\beta_N$ , and 3) other parameters, such as line-averaged electron density ( $n_{e,l}$ ) and plasma shape, have little correlation with  $\beta_N$ . In almost all KSTAR suppression cases in the database,  $\beta_N$  is below 2.4. Therefore, the lower limit of target  $\beta_N$  for plasma performance enhancement is set at 2.4.

For efficient  $\beta_N$  enhancement, the integrated RMP-based ELM-crash-control process incorporates the latest achievements related to the RMP technique. The integrated process applies the ERMP, favorable to the plasma confinement due to the reduced resonant components inside the edge region while maintaining the edge component above the suppression threshold, at the time of L–H transition using the real-time ML classifier. The ML-based pre-emptive RMP onset, triggering RMP before the first ELM crash of H-mode, reduces the external heating power required to achieve the same  $\beta_N$  by over 10% compared to the conventional RMP onset according to the pre-set control parameter. After taking over  $I_{RMP}$  control authority from the ML classifier, the adaptive feedback RMP ELM controller optimizes the  $I_{RMP}$  level to enhance  $\beta_N$  during the suppression phase and sustain the  $\beta_N$ -enhanced suppression state. The performance of the integrated process is experimentally validated. The integrated process maintains the  $\beta_N > 2.4$  suppression phase for  $\sim 4$  s ( $\sim 60\tau_E$ ) and achieves  $\beta_N$  up to  $\sim 2.65$  during the suppression phase, which is  $\sim 10\%$  higher than the previous KSTAR record, but  $\sim 6\%$  lower than the target of K-DEMO first phase. Furthermore, the integrated process confirms the additional advantage of the ERMP spectrum on top of its contribution to the  $\beta_N$  enhancement. During the adaptive control, the restoration time for the suppression phase and the recovery time for  $\beta_N \sim 2.6$  suppression are reduced by  $\sim 38\%$ – $62\%$  and  $\sim 51\%$ , respectively, in the ERMP compared to the CRMP when the ELM-crash-mitigation phase accompanied by a drop in  $\beta_N$  occurs.

A series of post-analyses provide several findings that 1) the evolution of  $\beta_N$  is predominantly influenced by electron temperature, 2) the onset of  $\beta_N$  recovery after the mitigation phase accompanied by a temporary  $\beta_N$  drop may be related to the repetition frequency of mitigated ELM crashes, and 3) the impact of the ERMP spectrum is more radially localized to the edge of the plasma compared to the CRMP spectrum.







## Acknowledgments

The authors thank all the KSTAR team members for their support. This research was supported by the R&D Program of ‘KSTAR Experimental Collaboration and Fusion Plasmas Research (EN2301-14)’ through the Korea Institute of Fusion Energy (KFE) funded by Government funds, and by the KOREA HYDRO & NUCLEAR POWER CO., LTD (No. 2019-Tech-G19IO16). This material was supported by the



U.S. Department of Energy under Awards DE-SC0020372. This work was also supported by the U.S. Department of Energy under contract number DEAC02-09CH11466 (Princeton Plasma Physics Laboratory).

## ORCID iDs

Minwoo Kim  <https://orcid.org/0000-0002-8627-4584>  
 G. Shin  <https://orcid.org/0000-0002-7925-3208>  
 J. Lee  <https://orcid.org/0000-0002-0852-8817>  
 H. Han  <https://orcid.org/0000-0001-6506-9824>  
 S.-H. Hahn  <https://orcid.org/0000-0001-8115-9248>  
 S.K. Kim  <https://orcid.org/0000-0002-0701-8962>  
 S.M. Yang  <https://orcid.org/0000-0003-1214-1268>  
 R. Shousha  <https://orcid.org/0000-0003-1498-8980>  
 J.-W. Juhn  <https://orcid.org/0000-0002-9435-4349>

## References

- [1] Loarte A. et al 2014 Progress on the application of ELM control schemes to ITER scenarios from the non-active phase to DT operation *Nucl. Fusion* **54** 033007
- [2] Evans T.E. et al 2004 Suppression of large edge-localized modes in high-confinement DIII-D plasmas with a stochastic magnetic boundary *Phys. Rev. Lett.* **92** 235003
- [3] Evans T.E. 2015 Resonant magnetic perturbations of edge-plasmas in toroidal confinement devices *Plasma Phys. Control. Fusion* **57** 123001
- [4] Jeon Y.M. et al 2012 Suppression of edge localized modes in high-confinement KSTAR plasmas by nonaxisymmetric magnetic perturbations *Phys. Rev. Lett.* **109** 035004
- [5] Lee J., Yun G.S., Choi M.J., Kwon J.-M., Jeon Y.-M., Lee W., Luhmann N.C. Jr and Park H.K. 2016 Nonlinear interaction of edge-localized modes and turbulent eddies in toroidal plasma under  $n = 1$  magnetic perturbation *Phys. Rev. Lett.* **117** 075001
- [6] Hahn S.-H. et al 2021 Exploration of RMP ELM control on ITER-similar shape (ISS) in KSTAR *Nucl. Fusion* **61** 126026
- [7] Evans T.E. et al 2005 Suppression of large edge localized modes with edge resonant magnetic fields in high confinement DIII-D plasmas *Nucl. Fusion* **45** 595
- [8] Moyer R.A. et al 2005 Edge localized mode control with an edge resonant magnetic perturbation *Phys. Plasmas* **12** 056119
- [9] Paz-Soldan C., Nazikian R., Cui L., Lyons B.C., Orlov D.M., Kirk A., Logan N.C., Osborne T.H., Suttrop W. and Weisberg D.B. 2019 The effect of plasma shape and neutral beam mix on the rotation threshold for RMP-ELM suppression *Nucl. Fusion* **59** 056012
- [10] Suttrop W. et al 2011 First observation of edge localized modes mitigation with resonant and nonresonant magnetic perturbations in ASDEX Upgrade *Phys. Rev. Lett.* **106** 225004
- [11] Suttrop W. et al 2018 Experimental conditions to suppress edge localised modes by magnetic perturbations in the ASDEX Upgrade tokamak *Nucl. Fusion* **58** 096031
- [12] Sun Y. et al 2016 Nonlinear transition from mitigation to suppression of the edge localized mode with resonant magnetic perturbations in the EAST tokamak *Phys. Rev. Lett.* **117** 115001
- [13] In Y. et al 2017 Enhanced understanding of non-axisymmetric intrinsic and controlled field impacts in tokamaks *Nucl. Fusion* **57** 116054
- [14] Kim M. et al 2020 Pedestal electron collisionality and toroidal rotation during ELM-crash suppression phase under  $n = 1$  RMP in KSTAR *Phys. Plasmas* **27** 112501
- [15] Kim S. et al 2022 Optimization of 3D controlled ELM-free state with recovered global confinement for KSTAR with  $n = 1$  resonant magnetic field perturbation *Nucl. Fusion* **62** 026043
- [16] Unterberg E.A., Evans T.E., Maingi R., Brooks N.H., Fenstermacher M.E., Mordijck S. and Moyer R.A. 2009 Demonstration of particle exhaust control during ELM suppression by resonant magnetic perturbations in DIII-D *Nucl. Fusion* **49** 092001
- [17] Mordijck S. et al 2012 Changes in particle transport as a result of resonant magnetic perturbations in DIII-D *Phys. Plasmas* **19** 056503
- [18] McKee G.R. et al 2013 Increase of turbulence and transport with resonant magnetic perturbations in ELM-suppressed plasmas on DIII-D *Nucl. Fusion* **53** 113011
- [19] Nazikian R. et al 2021 Pedestal collapse by resonant magnetic perturbations *Nucl. Fusion* **61** 044001
- [20] Valovič M. et al 2016 Pellet refuelling of particle loss due to ELM mitigation with RMPs in the ASDEX Upgrade tokamak at low collisionality *Nucl. Fusion* **56** 066009
- [21] Kirk A. et al 2010 Resonant magnetic perturbation experiments on MAST using external and internal coils for ELM control *Nucl. Fusion* **50** 034008
- [22] Kirk A. et al 2015 Effect of resonant magnetic perturbations on low collisionality discharges in MAST and a comparison with ASDEX Upgrade *Nucl. Fusion* **55** 043011
- [23] Wang S.X. et al 2018 Investigation of RMP induced density pump-out on EAST *Nucl. Fusion* **58** 112013
- [24] Hou J. et al 2019 Density compensation and stored energy recovery in resonant magnetic perturbation suppressed edge-localized mode H-mode plasmas using pellet fueling on EAST *Nucl. Fusion* **59** 096039
- [25] Hu Q.M., Nazikian R., Grierson B.A., Logan N.C., Park J.-K., Paz-Soldan C. and Yu Q. 2019 The density dependence of edge-localized-mode suppression and pump-out by resonant magnetic perturbations in the DIII-D tokamak *Phys. Plasmas* **26** 120702
- [26] Hu Q.M., Nazikian R., Grierson B.A., Logan N.C., Paz-Soldan C. and Yu Q. 2020 The role of edge resonant magnetic perturbations in edge-localized-mode suppression and density pump-out in low-collisionality DIII-D plasmas *Nucl. Fusion* **60** 076001
- [27] Sinha P., Ferraro N.M. and Belli E. 2022 Neoclassical transport due to resonant magnetic perturbations in DIII-D *Nucl. Fusion* **62** 126028
- [28] Han H. et al 2016 Versatile controllability of non-axisymmetric magnetic perturbations in KSTAR experiments *Fusion Eng. Des.* **108** 60–66
- [29] Park J.-K. et al 2013 Rotational resonance of nonaxisymmetric magnetic braking in the KSTAR tokamak *Phys. Rev. Lett.* **111** 095002
- [30] Park J.-K., Yang S.M., Logan N.C., Hu Q., Zhu C., Zarnstorff M.C., Nazikian R., Paz-Soldan C., Jeon Y.M. and Ko W.H. 2021 Quasisymmetric optimization of nonaxisymmetry in tokamaks *Phys. Rev. Lett.* **126** 125001
- [31] Kim K. et al 2017 Observation of resonant and non-resonant magnetic braking in the  $n = 1$  non-axisymmetric configurations on KSTAR *Nucl. Fusion* **57** 126035
- [32] Paz-Soldan C. et al (DIII-D Team) 2021 Plasma performance and operational space without ELMs in DIII-D *Plasma Phys. Control. Fusion* **63** 083001
- [33] Kang J.S., Park J.M., Jung L., Kim S.K., Wang J., Lee C.Y., Na D.H., Im K., Na Y.-S. and Hwang Y.S. 2017 Development of a systematic, self-consistent algorithm for the K-DEMO steady-state operation scenario *Nucl. Fusion* **57** 126034



- [34] Wenninger R. *et al* 2016 The physics and technology basis entering european system code studies for DEMO *Nucl. Fusion* **57** 016011
- [35] Asakura N. *et al* 2017 Studies of power exhaust and divertor design for a 1.5 GW-level fusion power DEMO *Nucl. Fusion* **57** 126050
- [36] Shin G., Juhn J.-W., Kwon G.I. and Hahn S.-H. 2020 Real-time classification of L-H transition and ELM in KSTAR *Fusion Eng. Des.* **157** 111634
- [37] Shin G. *et al* 2022 Preemptive RMP-driven ELM crash suppression automated by a real-time machine-learning classifier in KSTAR *Nucl. Fusion* **62** 026035
- [38] Shousha R. *et al* 2022 Design and experimental demonstration of feedback adaptive RMP ELM controller toward complete long pulse ELM suppression on KSTAR *Phys. Plasmas* **29** 032514
- [39] Shousha R. *et al* 2023 ELM-suppressed H-mode operations with adaptive ELM control on DIII-D and KSTAR *Nucl. Fusion* submitted
- [40] Yang S.M. *et al* 2020 Localizing resonant magnetic perturbations for edge localized mode control in KSTAR *Nucl. Fusion* **60** 096023
- [41] Yang S.M. *et al* 2023 Tailoring error field of tokamak to control plasma instability and transport (<https://doi.org/10.21203/rs.3.rs-2617922/v1>)
- [42] In Y. *et al* 2019 Tamed stability and transport using controlled non-axisymmetric fields in KSTAR *Nucl. Fusion* **59** 056009
- [43] In Y., Loarte A., Lee H.H., Kim K., Jeon Y.M., Park J.-K., Ahn J.-W., Park G.Y., Kim M. and Park H. 2019 Test of the ITER-like resonant magnetic perturbation configurations for edge-localized mode crash suppression on KSTAR *Nucl. Fusion* **59** 126045
- [44] In Y. *et al* 2022 Toward holistic understanding of the ITER-like resonant magnetic perturbation (RMP) ELM control on KSTAR *Nucl. Fusion* **62** 066014
- [45] Lee J., Jeon Y.M., In Y., Park G.Y., Yun G.S., Lee W., Kim M., Lee J.H., Ko W.H. and Park H.K. 2019 Direct evidence of  $E \times B$  flow changes at the onset of resonant magnetic perturbation-driven edge-localized mode crash suppression *Nucl. Fusion* **59** 066033
- [46] Park J.-K. *et al* 2018 3D field phase-space control in tokamak plasmas *Nat. Phys.* **14** 1223–8
- [47] Lao L.L., St John H., Stambaugh R.D., Kellman A.G. and Pfeiffer W. 1985 Reconstruction of current profile parameters and plasma shapes in tokamaks *Nucl. Fusion* **25** 1611
- [48] Nam Y.U. and Lee K.D. 2008 A 280 GHz single-channel millimeter-wave interferometer system for KSTAR *Rev. Sci. Instrum.* **79** 10E705
- [49] Juhn J.-W., Lee K.C., Lee T.G., Wi H.M., Kim Y.S., Hahn S.H. and Nam Y.U. 2021 Multi-chord IR–visible two-color interferometer on KSTAR *Rev. Sci. Instrum.* **92** 043559
- [50] McDermott R.M., Angioni C., Dux R., Gude A., Pütterich T., Ryter F. and Tardini G. (ASDEX Upgrade Team) 2011 Effect of electron cyclotron resonance heating (ECRH) on toroidal rotation in ASDEX Upgrade H-mode discharges *Plasma Phys. Control. Fusion* **53** 035007
- [51] Lee S.G. 2020 Influence of toroidal rotation from electron cyclotron resonance heating in KSTAR *Phys. Plasmas* **27** 064503
- [52] Gu S. *et al* 2022 Influence of triangularity on the plasma response to resonant magnetic perturbations *Nucl. Fusion* **62** 076031
- [53] Ryan D.A., Liu Y.Q., Li L., Kirk A., Dunne M., Dudson B., Piovesan P., Suttrop W. and Willensdorfer M. (ASDEX Upgrade Team) 2017 Numerically derived parametrisation of optimal RMP coil phase as a guide to experiments on ASDEX Upgrade *Plasma Phys. Control. Fusion* **59** 024005
- [54] Fitzpatrick R. and Hender T.C. 1991 The interaction of resonant magnetic perturbations with rotating plasmas *Phys. Fluids B* **3** 644–73
- [55] Park J.-K., Boozer A.H. and Glasser A.H. 2007 Computation of three-dimensional tokamak and spherical torus equilibria *Phys. Plasmas* **14** 052110
- [56] Kim H.-S. *et al* 2014 Characteristics of global energy confinement in KSTAR L- and H-mode plasmas *Nucl. Fusion* **54** 083012
- [57] Snyder P. *et al* 2019 High fusion performance in Super H-mode experiments on Alcator C-Mod and DIII-D *Nucl. Fusion* **59** 086017
- [58] Jeong S.H., Kim I.Y. and Hwang C.K. 2003 Design of a heterodyne electron cyclotron emission system on KSTAR *Rev. Sci. Instrum.* **74** 1433–6
- [59] Suttrop W. 2000 The physics of large and small edge localized modes *Plasma Phys. Control. Fusion* **42** A1
- [60] Yun G.S. *et al* 2014 Quasi 3D ECE imaging system for study of MHD instabilities in KSTAR *Rev. Sci. Instrum.* **85** 11D820
- [61] Sung C. *et al* 2013 Changes in core electron temperature fluctuations across the ohmic energy confinement transition in Alcator C-Mod plasmas *Nucl. Fusion* **53** 083010
- [62] Watts C. 2007 A review of ECE correlation radiometry techniques for detection of core electron temperature fluctuations *Fusion Sci. Technol.* **52** 176–92
- [63] Bornatici M., Cano R., De Barbieri O. and Engelmann F. 1983 Electron cyclotron emission and absorption in fusion plasmas *Nucl. Fusion* **23** 1153
- [64] Heyn M.F., Ivanov I.B., Kasilov S.V., Kernbichler W., Leitner P., Nemov V.V. and Suttrop W. (ASDEX Upgrade Team) 2014 Quasilinear modelling of RMP interaction with a tokamak plasma: application to ASDEX Upgrade ELM mitigation experiments *Nucl. Fusion* **54** 064005
- [65] Hahn T.S., Kim Y.J., Diamond P.H. and Choi G.J. 2021 Anisotropic  $E \times B$  shearing rate in a magnetic island *Phys. Plasmas* **28** 022302
- [66] Eldon D. *et al* 2022 Enhancement of detachment control with simplified real-time modelling on the KSTAR tokamak *Plasma Phys. Control. Fusion* **64** 075002
- [67] Wang L. *et al* 2022 Achievements of actively controlled divertor detachment compatible with sustained high confinement core in DIII-D and EAST *Nucl. Fusion* **62** 076002
- [68] Jia M. *et al* 2021 Integrated ELM and divertor power flux control using RMPs with low input torque in EAST in support of the ITER research plan *Nucl. Fusion* **61** 106023
- [69] Shin H., Hwang J., Han Y., Shin G., Lee H., Chai K.-B. and Choe W. 2023 Argon-seeded detachment during ELM control by RMPs in KSTAR *Nucl. Fusion* **63** 044003